COMPDYN 2013
4th ECCOMAS Thematic Conference on
Computational Methods in Structural Dynamics and Earthquake Engineering
M. Papadrakakis, V. Papadopoulos, V. Plevris (eds.)
Kos Island, Greece, 12–14 June 2013

MINIMAL-DAMAGE STEEL FRAMES USING POST-TENSIONED CONNECTIONS WITH WEB HOURGLASS SHAPE PINS: DESIGN AND ASSESSMENT

Athanasios I. Dimopoulos[1], Theodore L. Karavasilis[1], George Vasdravellis[2] and Brian Uy[2]

[1] School of Engineering, University of Warwick
CV4 7AL, Coventry, United Kingdom
e-mail: {A.Dimopoulos,T.Karavasilis}@warwick.ac.uk

[2] Institute for Infrastructure Engineering, University of Western Sydney
Penrith NSW 2751, Sydney, Australia
{G.Vasdravellis,B.Uy}@uws.edu.au

Keywords: Self-centering, Post-tensioned, Seismic Design, Steel connection, Steel MRFs.

Abstract. *A new self-centering steel post-tensioned connection using web hourglass shape steel pins (WHPs) has been recently developed and experimentally validated. The connection isolates inelastic deformations in WHPs, avoids damage in other connection parts as well as in beams and columns, and eliminates residual drifts. WHPs do not interfere with the composite slab and can be very easily replaced without bolting or welding, and so, the connection enables non-disruptive repair and rapid return to building occupancy in the aftermath of a strong earthquake. This paper presents a simplified nonlinear model for the connection and the associated beams and columns that consists of nonlinear beam-column elements, and hysteretic and contact zero-length spring elements appropriately placed in the beam-column interface. The model was calibrated against experimental results and found to accurately simulate the connection behaviour. A prototype building was selected and designed as a conventional steel moment-resisting frame (MRF) according to Eurocode 8 or as a self-centering steel MRF (SC-MRF) using the connection with WHPs. Seismic analyses results show that the conventional MRF and the SC-MRF have comparable peak storey drifts, and highlight the inherent potential of the SC-MRF to eliminate damage in beams and residual drifts. The paper also shows that repair of damage in the conventional MRF will be costly and disruptive after the design basis earthquake, and, not financially viable after the maximum considered earthquake due to large residual drifts.*

1 INTRODUCTION

Conventional ductile steel moment-resisting frames (MRFs) are currently designed to form a global plastic mechanism under strong earthquakes by developing plastic hinges at the ends of the beams and at the base of the columns [7]. This design approach results in softening force-drift behaviour, and so, has many advantages including reduced member forces and low base shear force. However, plastic hinges in structural members involve cyclic inelastic deformations and local buckling which result in difficult to inspect and repair damage as well as residual drifts. The socio-economic losses related to damage and residual drifts are repair costs, loss of building occupation and business interruption, and possibly building demolition due to the complications associated with repairing large residual drifts [19].

A challenge of modern earthquake engineering is the development, standardization and practical implementation of resilient minimal-damage structures having the inherent potential to overcome the socio-economic losses related to earthquake damage by minimizing or avoiding inelastic deformations and residual drifts. Examples of minimal damage steel structures include frames equipped with rate-dependent passive dampers [12, 13, 27], frames with steel energy dissipation devices [14], and, self-centering moment-resisting frames (SC-MRFs) with post-tensioned (PT) connections.

SC-MRFs exhibit softening force-drift behaviour while eliminating inelastic deformations and residual drifts under strong earthquakes as the result of gap openings developed in beam-to-column interfaces and self-centering capability due to elastic pre-tensioning elements (e.g., high strength steel bars) which clamp beams to the columns. PT connections use carefully designed energy dissipation devices which are activated when gaps open and can be classified into yielding devices which dissipate energy through inelastic deformations and devices which dissipate energy through friction. Yielding devices were proposed as angles bolted on the top and bottom flanges of the beam and on the column flanges, dissipating energy through inelastic bending [20, 21, 10]; buckling-restrained steel bars placed between the beam flanges and welded on the beam and column, dissipating energy through axial deformations [6]; reduced flange plates welded around a square-hollow-section column and bolted on the beam flanges [3]; and reduced-section or cross-shaped steel plates placed below the bottom flange of the beam [4]. Friction-based devices were proposed as friction bolted surfaces placed on the top and bottom flanges of the beam [22, 15], on the web of the beam [24] or on the bottom flange of the beam [28, 16].

A new steel PT connection using web hourglass shape steel pins (WHPs) has been recently developed, modeled in ABAQUS and experimentally validated [25, 26]. The connection isolates inelastic deformations in WHPs, avoids damage in other connection parts as well as in beams and columns, and, eliminates residual drifts. WHPs do not interfere with the composite slab and are very easy-to-replace without bolting or welding, and so, the connection enables non-disruptive repair and rapid return to building occupancy in the aftermath of a strong earthquake.

This paper presents a simplified nonlinear model for the PT connection with WHPs and the associated beams and columns that consists of nonlinear beam-column elements, and hysteretic and contact zero-length spring elements appropriately placed in the beam-column interface. The model was calibrated against experimental results and found to accurately simulate the connection behaviour. A prototype building was selected and designed as a conventional steel MRF according to [8] or as a steel SC-MRF using PT connections with WHPs. The design process resulted in the same beam and column cross sections for the conventional MRF and the SC-MRF, while WHPs and the required beam flange reinforcing plates of the SC-MRF have practical sizes. Nonlinear models for the conventional MRF and the SC-MRF were de-

veloped in OpenSees [18] and used to conduct seismic analyses that show that the conventional MRF and the SC-MRF have comparable peak storey drifts. The SC-MRF eliminates damage in beams and residual drifts, and so, avoids disruptive repair after the design basis earthquake (DBE) and the maximum considered earthquake (MCE). On the other hand, repair of damage in the conventional MRF will be costly and disruptive after the DBE, and, not financially viable after the MCE due to large residual drifts.

2 STEEL POST-TENSIONED CONNECTION WITH WHPS

2.1 Structural details

Fig. 1 shows a schematic representation of a SC-MRF incorporating PT connections with WHPs and the details of an exterior PT connection. Two high strength steel bars located at the mid-depth of the beam, one at each side of the web, pass through holes drilled on the column flanges. The bars are post-tensioned and anchored to the exterior column flange, and so, clamp the beam to the column. Four WHPs are inserted in aligned holes drilled on the web of the beam and on strong supporting plates. The supporting plates are welded on the column flanges and have large thickness to provide fixed support boundary conditions to WHPs. Energy dissipation is provided by inelastic bending of the WHPs which are symmetrically placed (close to the top and bottom beam flange) to provide increased lever arm, and so, increased internal moment resistance. WHPs are designed to have an hourglass shape to provide enhanced energy dissipation and fracture capacity [17] as shown in Fig. 2. Both sides of the beam web are reinforced with steel plates to increase the contact surface of the WHPs with the web. In that way, possible ovalization of the holes drilled on the web and the reinforcing plates under the WHP bearing forces will be negligible and pronounced pinching behavior under cyclic deformations can be avoided. The connection includes beam flange reinforcing plates to avoid excessive early yielding in the beam flanges under the high PT bars forces. In addition, the panel zone is strengthened with doubler and continuity plates.

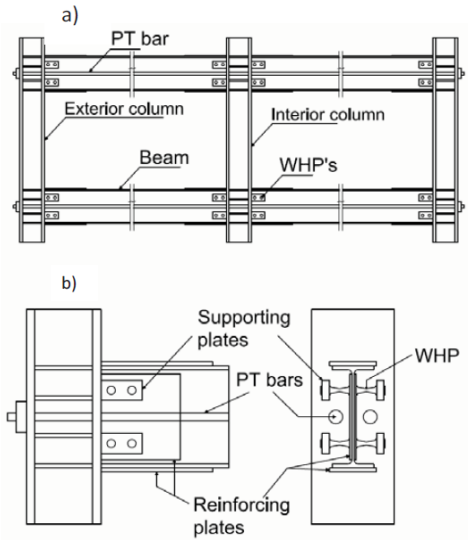

Figure 1: (a) SC-MRF incorporating PT connections with WHPs; (b) exterior PT connection details.

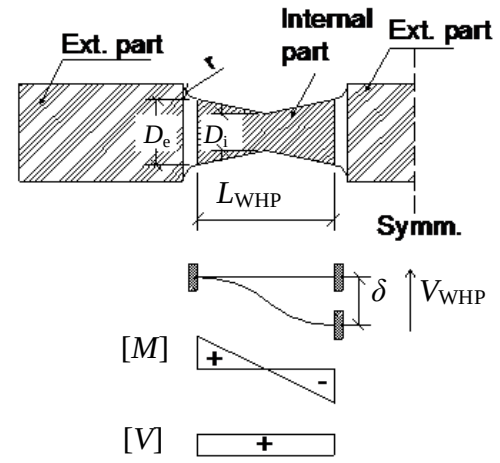

Figure 2: Geometry of half a WHP, assumed static system, and internal forces diagrams.

2.2 Theoretical analysis of cyclic behaviour

The connection behavior is characterized by gap opening and closing in the beam-column interface as a result of the re-centering force in the PT bars. Fig. 3 shows the gap opening mechanism in the connection where d_{1u} and d_{1l} are the distances of the upper and lower WHPs from the center of rotation (COR), respectively; d_2 is the distance of the PT bars from the COR; F_{PT} is the total force in both PT bars; $F_{WHP,u}$ and $F_{WHP,l}$ are the forces in the upper and lower WHPs, respectively; and CF is the compressive force on the beam-column bearing surface. It is assumed that the COR is located at the inner edge of the beam flange reinforcing plate. This assumption has been verified by the large-scale experiments previously conducted by [25].

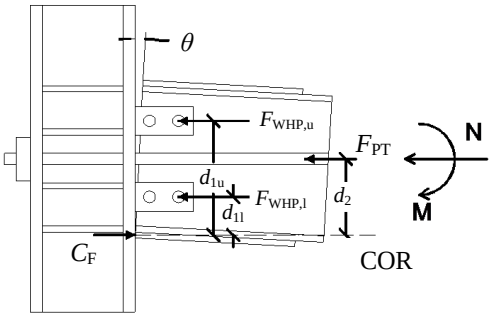

Figure 3: Gap opening mechanism in a PT connection with WHPs

Fig. 4 shows the assumed bilinear elastoplastic force-displacement ($F_{WHP,i}$-δ) behavior of one of the four (i=1 to 4) WHPs, while Fig. 5 shows the assumed cyclic moment-rotation (M-θ) behavior of the connection. M is the sum of the moment contributions from the PT bars, M_{PT}, and the WHPs, M_{WHP}. Fig. 5(b) shows the nonlinear elastic moment contribution of both PT bars. In Fig. 5(b), M_d is the decompression moment, i.e., equal to $F_{PT,i} \cdot d_2$, where $F_{PT,i}$ is the total initial post-tensioning force in both PT bars. Fig. 5(c) shows the moment contribution of the four WHPs. The M_{WHP}-θ curve changes slope two times since the upper WHPs yield at a rotation θ_2 and the lower WHPs yield afterwards at rotation θ_3. Point 1 in Fig. 5(a) corresponds to the decompression moment, M_d, of the connection. After decompression, gap opens and the connection behavior becomes nonlinear elastic. The stiffness K_1 between points 1 and

2 is equal to the sum of the rotational stiffness contribution of the PT bars, K_{PT}, and the rotational stiffness contribution of the WHPs, K_e:

$$K_1 = K_{pT} + K_e = \frac{K_{PT,a}K_b}{K_{PT,a}+K_b} d_2^2 + 2K_{fe}(d_{1l}^2 + d_{1u}^2) \quad (1)$$

where K_{fe} is the elastic stiffness of the force-displacement relationship of one WHP shown in Fig. 4, $K_{pt,a}$ is the total axial elastic stiffness of both PT bars, and K_b is the axial elastic stiffness of the beam. At point 2, the upper WHPs yield and M continues to increase with slope K_2:

$$K_2 = K_{pT} + K_{p1} = \frac{K_{PT,a}K_b}{K_{PT,a}+K_b} d_2^2 + 2(K_{fe}d_{1l}^2 + K_{fp}d_{1u}^2) \quad (2)$$

where K_{fp} is the post-elastic stiffness of the force-displacement relationship of one WHP shown in Fig. 4. At point 3, the lower WHPs yield and M continues to increase with slope K_3:

$$K_3 = K_{pT} + K_{p2} = \frac{K_{PT,a}K_b}{K_{PT,a}+K_b} d_2^2 + 2K_{fp}(d_{1l}^2 + d_{1u}^2) \quad (3)$$

When loading is reversed, the connection begins to unload, from point 4 to point 5, with the same elastic stiffness, K_1. After point 5, the connection unloads with stiffness equal to K_2 between points 5 and 6 and with stiffness K_3 between points 6 and 7 until the gap closes. The behavior of the connection is symmetric, since the WHPs are placed symmetrically to the beam centerline. The moment in the connection, M, is calculated as

$$M = M_{pT} + M_{WHP} \quad (4)$$

where M_{PT} is obtained as

$$M_{pT} = M_d + \frac{K_{PT,a}K_b}{K_{PT,a}+K_b} d_2^2\theta \quad (5)$$

and M_{WHP} is obtained as (see Fig. 3):

$$M_{WHP} = F_{WHP,u}d_{1u} + F_{WHP,l}d_{1l} \quad (6)$$

The assumed static system for half a WHP is shown in Fig. 2. The yield strength, V_{WHP}, of half a WHP is controlled either by the plastic moment of resistance, M_{pl}, or the plastic shear resistance, V_{pl} [8]:

$$M_{pl} = \frac{D_e^3}{6} f_y \quad (7)$$

$$V_{pl} = 0.9\frac{\pi D_i^2}{4} f_y/\sqrt{3} \quad (8)$$

where f_y is the yield strength of the WHP material, D_e is the equivalent external diameter (to be defined later), and D_i is the diameter at the mid-length of half a WHP, as indicated in Fig. 2. The factor 0.9 in Eq. 8 accounts for the relation between the average shear stress and the maximum shear stress in a circular section. The internal WHP part is connected to the external WHP part using a radius of 5 mm to avoid stress concentration and early fracture. It is assumed that D_e, which controls the WHP bending resistance, is equal to the diameter at the start of the round-shaped part with radius r. Plastic analysis assumes that the plastic moment of resistance should be reached at the ends before the plastic shear resistance is reached at the mid-length of half a WHP. By equilibrium, the aforementioned condition can be written as:

$$V_{\mathrm{WHP}} = \frac{2M_{\mathrm{Pl}}}{L_{\mathrm{WHP}}} < V_{\mathrm{pl}} \tag{9}$$

where L_{WHP} is the clear length of the bending parts of half a WHP. The yield force of a WHP, $F_{\mathrm{y,WHP}}$, is then calculated as:

$$F_{\mathrm{y,WHP}} = 2V_{\mathrm{WHP}} \tag{10}$$

Based on the virtual work method along with analytical integration, the elastic stiffness K_{fe} of a WHP is calculated as:

$$K_{\mathrm{fe}} = 2\frac{9\pi D_{\mathrm{e}}^{3} D_{\mathrm{i}} EG}{(40E D_{\mathrm{e}}^{2} L_{\mathrm{WHP}} + 48G L_{\mathrm{WHP}}^{3})} \tag{11}$$

where E is the modulus of elasticity and G the shear modulus of the WHPs material.

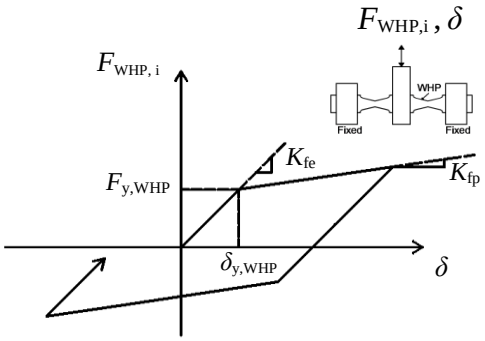

Figure 4: Assumed cyclic behaviour of one WHP

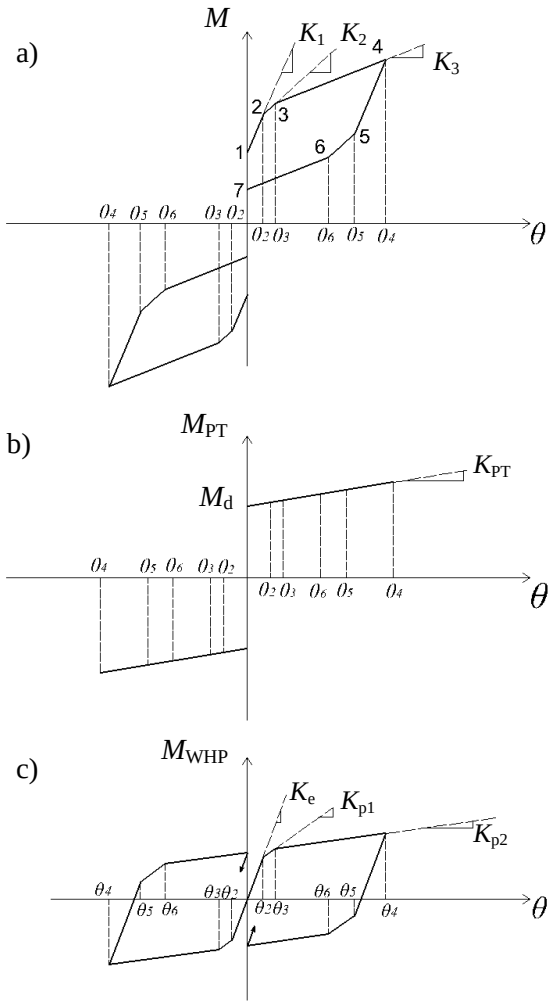

Figure 5: Assumed cyclic behaviour of a PT connection with WHPs

3 MODELING OF PT CONNECTION WITH WHPS FOR NONLINEAR ANALYSIS

3.1 Model development in OpenSees

A model for the PT connection with WHPs and the associated beams and columns was developed in OpenSees as shown in Fig. 6. The beams and columns were modeled using the nonlinear force-based beam-column fiber element which can strictly satisfy equilibrium and accurately capture the distribution of inelasticity along the depth of the section and along the length of the physical member. For the beam, two fiber elements with cross-sections having different flange thickness were used to account for the beam flange reinforcing plates. Each fiber was associated with uniaxial bilinear elastoplastic stress-strain behaviour (Steel01 in OpenSees) with a post-yield stiffness ratio equal to 0.01.

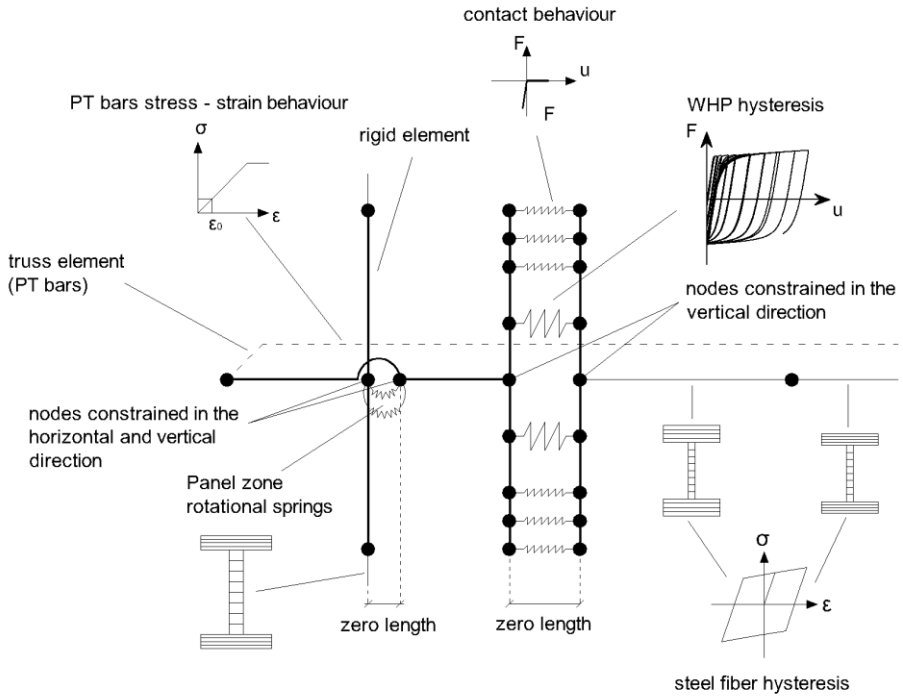

Figure 6: Model for an exterior PT connection with WHPs and associated columns and beam

Rigid elastic beam-column elements were used to model the beam-column interface where gap opening and closing takes place. To accurately capture the gap opening mechanism in the beam-column interface, three zero-length contact spring elements were placed at equal spaces along the beam flange thickness. These contact springs were associated with an elastic compression - no tension force-displacement behaviour (ENT material in Openness). A value of the compression stiffness equal to 20 times the axial stiffness of the beam K_b was assigned to these contact springs. Larger values for this stiffness were found to produce practically the same results but with higher computational cost, i.e., more iterations to achieve convergence and equilibrium in nonlinear analysis. To capture the hysteretic energy dissipation capacity of the connection, two zero-length hysteretic springs were placed at the exact locations of WHPs along the depth of the beam web. These springs were associated with a smooth hysteretic Giuffre-Menegotto-Pinto model with isotropic hardening (Steel 02 material in OpenSees).

To account for panel zone shear deformations and possible yielding, the panel zone was modeled using the Scissors model which introduces four additional rigid elastic beam-column elements and two nodes in the center of the panel zone connected with two zero-length rotational springs. Theses springs are associated with bilinear elastoplastic hysteretic rules (Steel01 material in OpenSees) with properties calculated to reflect the contribution of the column web (including doupler plates) and the column flanges in the shear force - shear deformation panel zone behaviour. This simple panel zone model has been found to produce identical results to those of the more computationally expensive Krawinkler panel zone model [2].

PT bars were modeled using a truss element running parallel to beam center-line axis and connected to the exterior nodes of the panel zones of the exterior columns of the SC-MRF. The truss element has a cross-section area A_{PT} equal to that of both PT bars. To account for post-tensioning, an initial strain equal to $F_{PT,i}/(A_{PT} \cdot E_{PT})$ was first assigned to the truss element where EP_T is the modulus of elasticity of the PT bar material. However, post-tensioning results in shortening of the beams which in turn decreases the post-tensioning force. To account

for this decrease, the initial strain in the truss element was increased to ensure that the post-tensioning force in the PT bars will be equal to $F_{PT,i}$ after the beam shortening.

3.2 Model calibration and assessment

The Steel02 OpenSees hysteretic model used for the WHP force-displacement behaviour was calibrated against experimental results from WHPs component tests previously conducted by Vasdravellis et al. (2012). Fig. 7.a shows the experimental setup for a pair of WHPs with the following properties: D_e=20 mm, D_i=14 mm, L_{WHP}=40 mm, f_y=560 MPa and E=200 GPa. Fig. 7.b compares and confirms a good agreement between the experimental hysteresis and the Steel02 hysteretic model. The Steel02 model has a yield strength equal to $2 \cdot F_{y,WHP}$; initial elastic stiffness equal to $0.6 \cdot (2 \cdot K_{fe})$; strain hardening ratio equal to 0.01; parameters controlling the transition from the elastic to inelastic regions of the hysteresis R_o=30, CR_1=0.925 and CR_2=0.15; and isotropic hardening parameters a_1=0.025, a_2=2.5, a_3=0.0 and a_4=1.0. The factor '2' for the calculation of the yield strength and stiffness reflects that a zero-length spring represents a pair of WHPs.

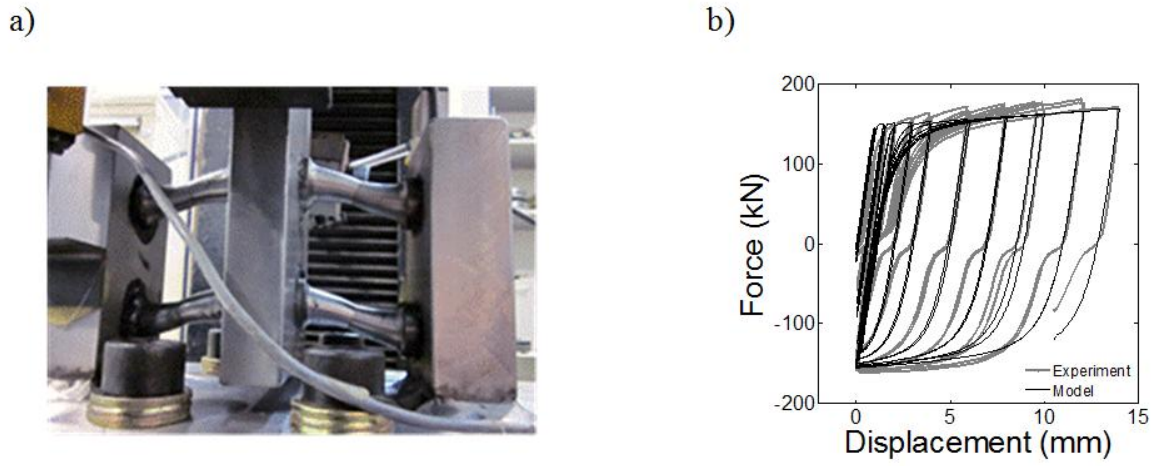

Figure 7: (a) Setup for WHP component tests; (b) comparison of experimental hysteresis and hysteretic model

The accuracy of the model for the PT connection with WHPs and the associated beams and columns (discussed in Section 3.1) was assessed using results from large-scale experimental tests previously conducted by Vasdravellis et al. (2012). Fig. 8.a shows the experimental test setup. A strong 310UC158 column was used along with two additional steel members welded to the column to form a truss system which increases the horizontal stiffness of the test setup. The whole system was bolted on the strong floor. The beam had a 250UB37 cross-section. The length of the beam flange reinforcing plates was 0.7 m. The total post-tensioning force was 504 kN. The displacement history was applied vertically by a hydraulic actuator positioned at a distance of 1800mm from the inner face of the column. The beam sections, column sections and beam flange reinforcing plates were made of steel with yield strength equal to 300 MPa. The WHPs were made of steel with yield strength equal to 560 MPa. The material of the PT bars had nominal yield strength equal to 930 MPa, tensile stress 1050 MPa and elongation capacity 6%, according to the specifications of the supplier. The loading protocol of [1] was used. This protocol consisted of three initial sets of six cycles at 6.75 mm, 9 mm, and 13.5 mm displacements, four subsequent cycles at 18 mm, and six sets of two cycles at 27,

36, and 54 mm. These displacements correspond to drifts equal to 0.00375, 0.005, 0.0075, 0.01, 0.015, 0.02, and 0.03. Fig. 8.b shows the experimental and analytical hysteresis for the PT connection and confirms a good agreement between the proposed model and the test results

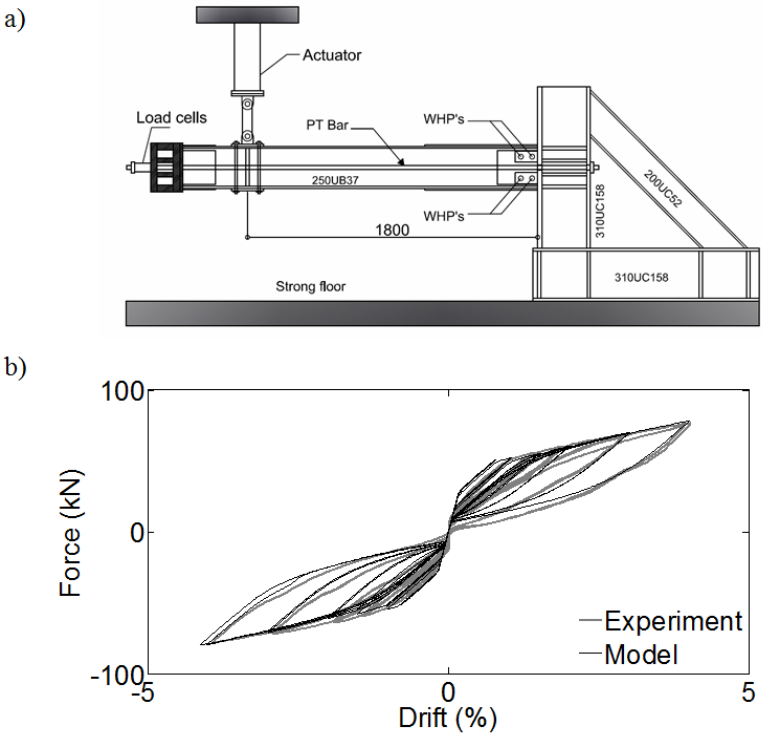

Figure 8: (a) Setup for WHP component tests; (b) comparison of experimental hysteresis and model in OpenSees

4 PROTOTYPE BUILDING

Fig. 9.a shows the plan view of the 5-storey, 4-bay by 3-bay prototype office building used for the study. The building has four identical MRFs to resist lateral loads in the longitudinal plan direction. The design study focused on one of the interior MRFs shown in Fig. 9.b. This MRF was designed either as a conventional steel MRF according to [7] or as a steel SC-MRF using PT connections with WHPs to compare their seismic performance. The dead and live gravity loads considered in the design are selected from [9]. The design seismic action, referred to herein as DBE, has a return period of 475 years and is expressed by the Type 1 elastic response spectrum of [7] with peak ground acceleration equal to 0.30g and ground type B (average shear wave velocity between 360 and 800 m/s.). The MRF was designed according to [8] and [7]. The steel yield strength for columns is assumed equal to 350 MPa and for beams equal to 300 MPa.

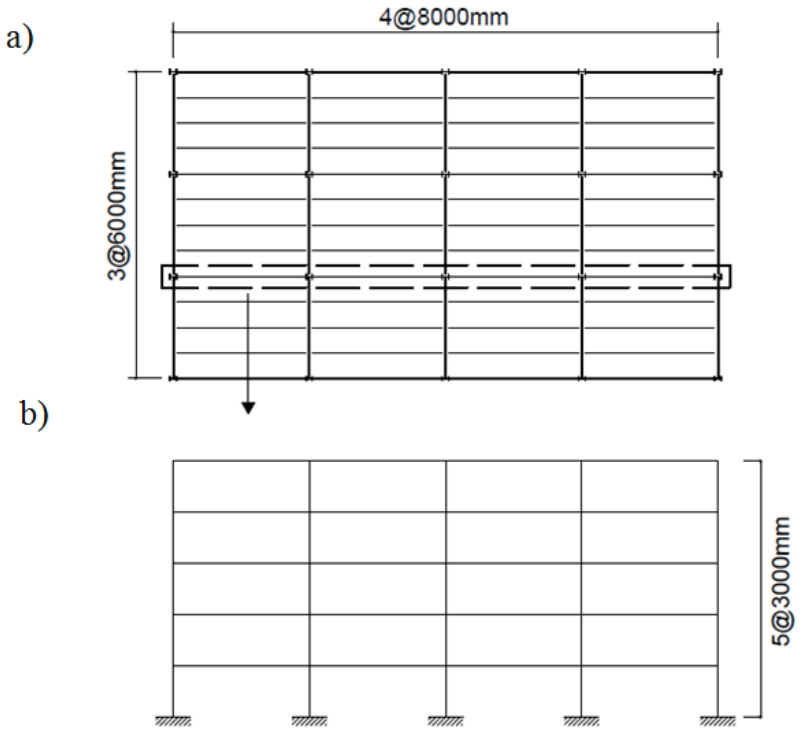

Figure 9: (a) Plan view of prototype building; (b) elevation of interior MRF

5 DESIGN OF THE CONVENTIONAL STEEL MRF

The model used to design the conventional steel MRF was based on the centerline dimensions of the MRF without accounting for the finite panel zone dimensions. The column base and beam-to-column connections were assumed to be fully rigid. A diaphragm constrain was imposed on the nodes of each floor to simulate the effect of the composite slab. The MRF was designed using the modal response spectrum analysis procedure of [7]. The MRF satisfied Ductility Class High [7] by using compact Class 1 cross-sections [8], and so, the behaviour (or 'strength reduction' for the USA) factor was set equal to $5 \cdot a_u/a_1=6.5$, where a_u/a_1 is the overstrength factor with a recommended value of 1.3 for multi-bay multi-storey steel MRFs. The displacement behavior (or 'displacement amplification' for the USA) factor is equal to q, i.e., [7] uses the equal displacement rule to estimate peak drifts associated with inelastic response. These drifts are then used to check second order (P-Δ) effects. Additionally, [7] uses a serviceability limit on the peak storey drift, $\theta_{s\text{-}max}$, under the frequently occurring earthquake (FOE) with a return period equal to 95 years. The FOE has intensity 40% (reduction factor v=0.4 in [7] the intensity of the DBE and the associated limit on $\theta_{s\text{-}max}$ was set equal to 0.75%, assuming ductile non-structural components. The MRF was designed to satisfy the strong column - weak beam capacity design rule of [7], the beam-to-column connections were designed to be fully rigid and the panel zones were strengthened with doubler and continuity plates to avoid yielding. A strength-based design with q=6.5 under the DBE was first performed. Beams and columns cross-sections from strength-based DBE design had to be increased to satisfy the serviceability 0.75% limit on $\theta_{s\text{-}max}$ under the FOE. The final sections were found iteratively by decreasing the value of q, designing the MRF for increased strength under the DBE and then checking storey drifts under the FOE. Table 1 lists the column cross-

sections and the beam cross-sections of the conventional MRF. The fundamental period of vibration is 1.08 s. and the estimated $\theta_{s\text{-}max}$ is 0.64% under the FOE, 1.6% under DBE and 2.4% under the MCE.

Storey	Cross sections MRF & SC-MRF		PT bars		WHPs			Reinf. plates	
	Beams	Columns	$F_{PT,I}$ (kN)	d_{PT} (mm)	D_e (mm)	D_i (mm)	L_{WHP} (mm)	L_{RP} (mm)	t_{RP} (mm)
1	IPE450	HEB400	933	36	36	26	65	1080	15
2	IPE450	HEB400	933	36	36	26	65	1080	15
3	IPE400	HEB400	806	36	33	23	65	1180	15
4	IPE400	HEB360	806	36	33	23	65	1180	15
5	IPE360	HEB360	700	36	32	22	65	1190	15

Table 1: Design details of the conventional steel MRF and the steel SC-MRF using PT connections with WHPs

6 DESIGN OF THE STEEL SC-MRF USING PT CONNECTIONS WITH WHPS

The sections of the conventional MRF were used for designing the SC-MRF so that both frames would have almost the same initial stiffness and fundamental period of vibration. The SC-MRF and the conventional MRF are expected to have similar drifts as it has been shown that self-centering and conventional bilinear elastoplastic systems of the same strength and period of vibration have similar drifts when the self-centering system is designed with adequate energy dissipation capacity and post-yield stiffness [12].

The PT connections with WHPs were designed using the methodology presented in [11] that adopts two performance objectives and associated structural limit states, namely: (1) Immediate Occupancy under the DBE by avoiding damage in beams and columns while permitting gap opening; and (2) Collapse Prevention under the MCE by avoiding PT bar yielding and beam local buckling while permitting minor yielding in beams. To initiate the design procedure, the moment corresponding to point 2 in Fig. 5.a, referred to herein as M_{IGO}, was set equal to 66% of the nominal plastic moment of resistance of the beam section. In addition, M_d was set equal to 69% of M_{IGO}. These M_{IGO} and M_d values provide an energy dissipation factor equal to 0.31 [11]. The post-tensioning force and the length of the reinforcing plates were then designed. PT bars were designed to avoid yielding for $\theta_{s\text{-}max} \leqslant 0.06$ rad. There was no need to increase the beam cross-sections to design the PT connections with WHPs. The design of the PT connections was based on $\theta_{s\text{-}max}$ values equal to 0.64% under the FOE, 1.6% under the DBE and 2.4% under the MCE, i.e., equal to those predicted for the conventional steel MRF. These drifts are significantly lower than those used in previous works which are based on the IBC 2% drift limit under the DBE [22, 11]. Table 1 lists the column cross-sections, beam cross-sections, $F_{PT,i}$, PT bar diameter d_{PT}, D_e, D_i, L_{WHP}, and length LRP and thickness t_{RP} of the beam flange reinforcing plates. The beam flange reinforcing plates are made of steel with yield strength equal to 300 MPa. The WHPs are made of steel with yield strength equal to 235 MPa. The material of the PT bars has nominal yield strength equal to 930 MPa and elongation capacity 6%. The fundamental period of vibration of the SC-MRF is 1.01 sec., i.e., slightly lower than that of the conventional MRF (1.08 sec) because the beam flange reinforcing plates increase the stiffness of the beams of the SC-MRF.

7 NONLINEAR MONOTONIC AND CYCLIC STATIC ANALYSIS

Fig. 10 shows the base shear coefficient (V/W) - roof drift (θ_r) behaviour of the conventional MRF and the SC-MRF from nonlinear monotonic (pushover) static analysis using nonlinear models described in Section 8.2. V is the base shear and W is the seismic weight. An inverted triangular force distribution along with roof displacement control was used in these analyses. The MRF and the SC-MRF have comparable base shear strengths and comparable initial stiffness. The pushover curves are plotted along with points associated with structural limit states and vertical lines corresponding to roof drifts expected under the FOE, DBE and MCE. The structural limit states for the conventional MRF are beam yielding and base column yielding and occur at θ_r equal to 0.82% and 0.92% respectively. The conventional MRF avoids damage under the FOE but experiences significant damage under the DBE. The structural limit states for the SC-MRF are decompression in a PT connection (i.e. point 1 in Fig. 5.a), WHP yielding (i.e. point 2 in Fig. 5.a), base column yielding and beam yielding. Fig. 10 shows that the beams of the SC-MRF are damage-free for θ_r equal or lower than 3%, i.e., drifts higher than the MCE. Damage in the SC-MRF is experienced at the column bases that yield at θ_r equal to 0.97%. No PT bar yielding is observed. The first decompression occurs at θ_r equal to 0.4% while WHPs yield at θ_r equal to 0.62% which is almost equal to the FOE drift. Decompression does not involve damage while yielding of the WHPs is acceptable under low drifts since WHPs can be easily replaced without bolting or welding. The conventional MRF experiences softening at θ_r equal to 1.25% while the SC-MRF shows a more gradual softening behaviour. In particular, the SC-MRF shows softening due to decompression in the PT connections at low drifts and further softening due to plastic deformations at the column bases and yielding of a large number of WHPs at θ_r equal to 1%. Fig. 11 shows the V/W - θ_r behaviour of the MRF and the SC-MRF from nonlinear cyclic (push-pull) static analysis. The first cycle of the analysis is performed up to the DBE drift while the next cycle up to the MCE drift. The SC-MRF shows full re-centering capability under the DBE, adequate energy dissipation and a small residual drift under the MCE due to plastic deformations at the column bases. The conventional MRF shows large energy dissipation capacity due to plastic deformations at the beam ends and at the column bases, and the possibility of experiencing large residual drifts under the DBE and MCE.

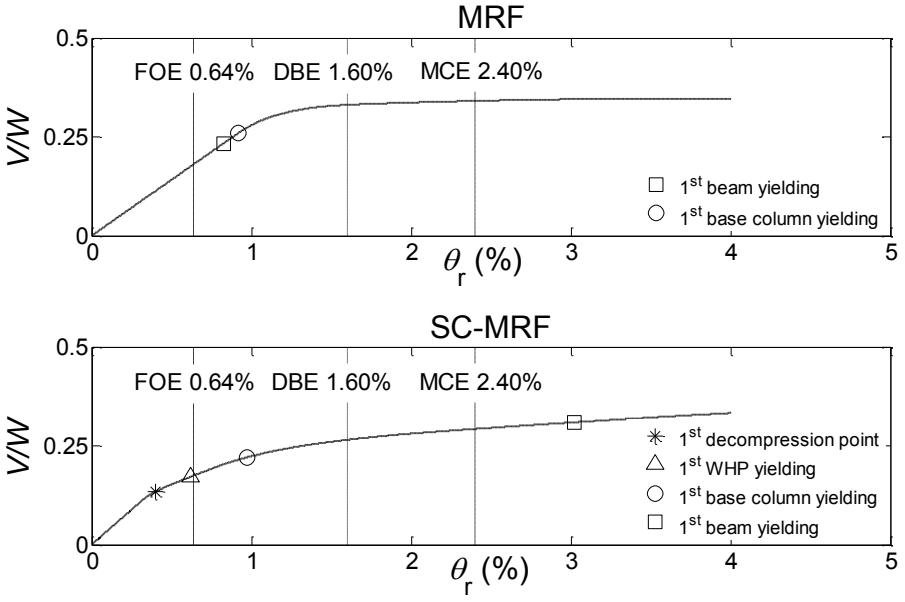

Figure 10: Base shear coefficient - roof drift behaviour from nonlinear monotonic (pushover) static analysis

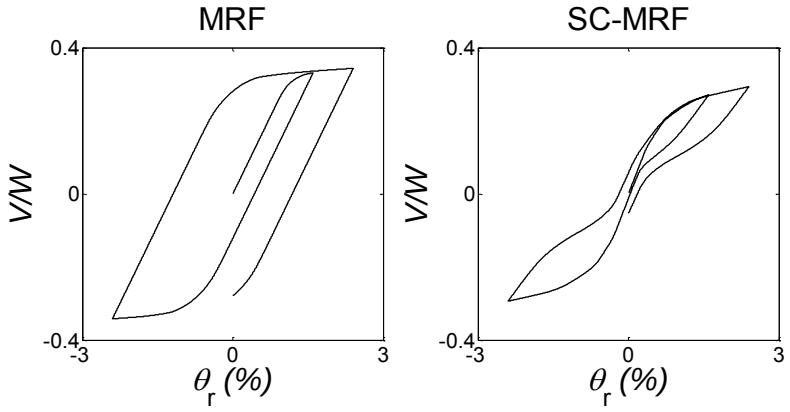

Figure 11: Base shear coefficient - roof drift behaviour from nonlinear cyclic (push-pull) static analysis

8 NONLINEAR DYNAMIC TIME HISTORY ANALYSES

8.1 Ground motions

A set of 20 earthquake ground motions recorded on ground type B were used in 2D nonlinear dynamic time history analyses to evaluate the performance of the SC-MRF and the performance of the conventional MRF. None of the ground motions exhibit near-fault forward directivity effects. The ground motions were scaled to the DBE level using the scaling procedure of [23]. Table 2 provides the scale factors and information on the 20 earthquake ground motions. Fig. 12 compares the DBE elastic response spectrum of [7] with the mean (μ) and mean plus/minus one standard deviation (μ±σ) spectra of the DBE ground motions. The amplitudes of the DBE ground motions were further scaled by 0.4 and 1.5 to represent FOE and MCE ground motions.

Earthquake	Station	Component	Magnitude (M_w)	Distance (km)	Scale factor		
					FOE	DBE	MCE
Imperial Valley 1979	Cerro Prieto	H-CPE237	6.53	15.19	0.82	2.05	3.08
Loma Prieta 1989	Hollister - S & P	HSP000	6.93	27.67	0.29	0.72	1.08
Loma Prieta 1989	Woodside	WDS000	6.93	33.87	1.40	3.49	5.24
Loma Prieta 1989	WAHO	WAH090	6.93	17.47	0.48	1.20	1.80
Manjil 1990	Abbar	ABBAR--T	7.37	12.56	0.28	0.70	1.05
Cape Mendocino 1992	Fortuna - Fortuna Blvd	FOR000	7.01	15.97	0.99	2.47	3.71
Cape Mendocino 1992	Rio Del Overpass - FF	RIO360	7.01	14.33	0.50	1.25	1.88
Landers 1992	Desert – Hot Springs	LD-DSP000	7.30	21.78	0.95	2.37	3.56
Northridge 1994	LA - W 15th St	W15090	6.69	25.60	1.14	2.86	4.29
Northridge 1994	Moorpark - Fire Sta	MRP180	6.69	16.92	0.78	1.94	2.91
Northridge 1994	N Hollywood - Cw	CWC270	6.69	7.89	0.53	1.33	2.00
Northridge 1994	Santa Susana Ground	5108-360	6.69	1.69	0.78	1.95	2.93
Northridge 1994	LA - Brentwood VA	0638-285	6.69	12.92	0.85	2.12	3.18
Northridge 1994	LA - Wadsworth VA	5082-235	6.69	14.55	0.62	1.54	2.31
Kobe 1995	Nishi-Akashi	NIS090	6.90	7.08	0.48	1.19	1.79
Kobe 1995	Abeno	ABN090	6.90	24.85	1.00	2.49	3.74
ChiChi 1999	TCU105	TCU105-E	7.62	17.18	0.96	2.39	3.59
ChiChi 1999	CHY029	CHY029-N	7.62	10.97	0.53	1.32	1.98
ChiChi 1999	CHY029	CHY041-N	7.62	19.83	0.56	1.40	2.10
Hector 1999	Hector	HEC090	7.13	10.35	0.42	1.04	1.56

Table 2: Properties of the ground motions used for nonlinear dynamic analyses

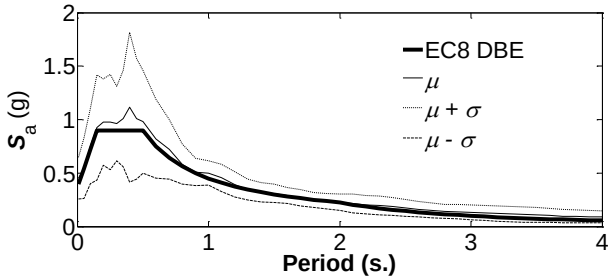

Figure 12: Comparison of the design EC8 spectrum with spectra of the ground motions used for nonlinear analyses

8.2 Modeling for nonlinear dynamic analysis

2D nonlinear analytical models of the conventional MRF and the SC-MRF were developed for nonlinear dynamic analyses in OpenSees. Nonlinear beam-column fiber elements were used for the beams and columns and the Scissors model [2] for the panel zones of the conventional MRF and the SC-MRF. A diaphragm constraint is imposed on each floor level of the conventional MRF. Stiff truss elements were used to connect the internal nodes of each bay of the SC-MRF to allow beam shortening due to post-tensioning, gap opening in PT connections, and to consider the use of a discontinuous slab proposed by [5]. The model of Fig. 6 was used to model the PT connections and the associated beams and columns of the SC-MRF.

The Newmark method with constant acceleration was used to integrate the equations of motion. The integration time step was selected to be 10 times smaller than the input time step of the earthquake ground motions. The Newton method with tangent stiffness was used to minimize the unbalanced forces within each integration time step of the nonlinear dynamic analysis. A Rayleigh damping matrix was used to model the inherent 3% critical damping at the first two modes of vibration. A nonlinear load controlled static analysis under the gravity loads was first performed, and then, the nonlinear dynamic time history analysis for each earthquake ground motion was executed. Each dynamic analysis was extended well beyond the actual earthquake time (the ground motions were padded with zeros) to allow for damped free vibration decay and accurate residual drifts calculation.

8.3 Seismic response results

Fig. 13 compares the roof drift time histories of the conventional MRF and the SC-MRF under the 5082-235 ground motion scaled to the DBE and MCE. Near the end of the time histories the SC-MRF oscillates around the origin, indicating negligible residual drift, while the conventional MRF experiences residual drifts. The peak roof displacements of the MRF and the SC-MRF are similar. Fig. 14 shows the stress-strain hysteresis at points A and B (extreme column base flange fibers), and, C and D (extreme beam flange fibers) of the first storey of the conventional MRF under the 5082-235 ground motion scaled to the DBE and MCE. Fig. 15 presents similar information for the SC-MRF. The stress-strain hysteresis immediately after the end of the beam flange reinforcing plate (points E and F) of the SC-MRF is also shown. The SC-MRF eliminates beam plastic deformations under both the DBE and MCE, while the conventional MRF experiences appreciable beam damage. Figs. 14 and 15 show that the column bases of the SC-MRF experience larger plastic deformations than those of the column bases of the conventional MRF.

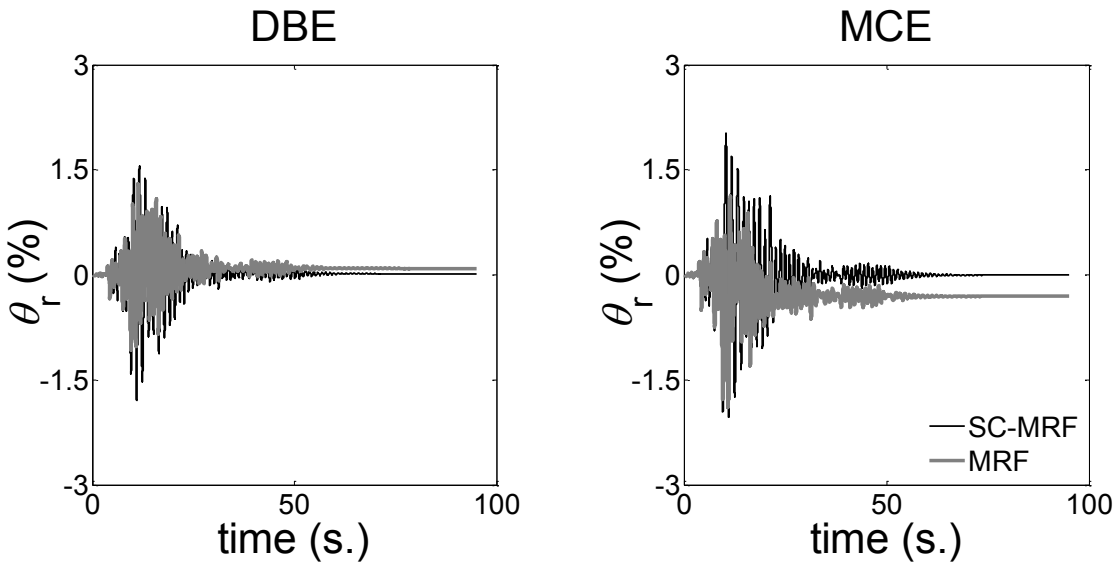

Figure 13: Comparison of the roof drift time histories under the 5082-235 ground motion scaled to the DBE and MCE

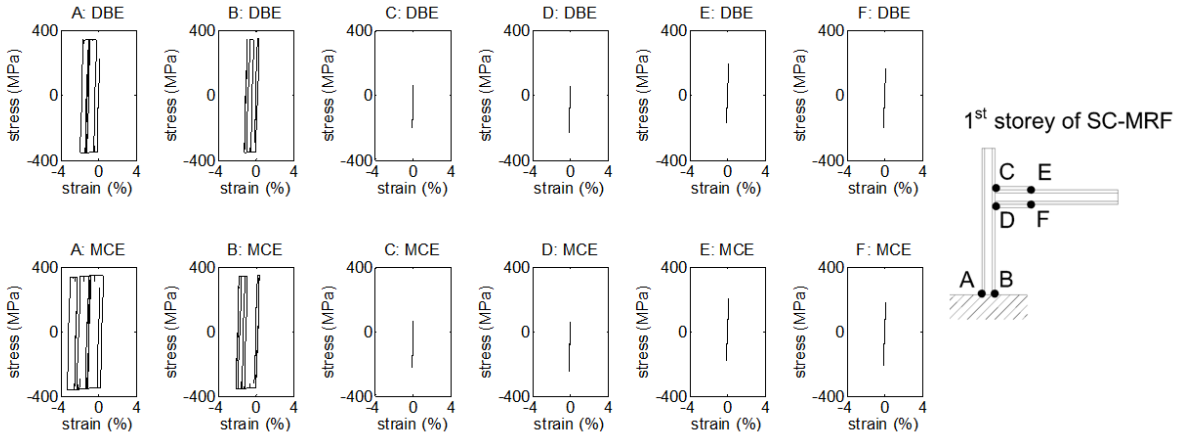

Figure 14: Stress-strain hysteresis at points A, B, C and D of the conventional MRF under the 5083-235 ground motion scaled at the DBE and MCE

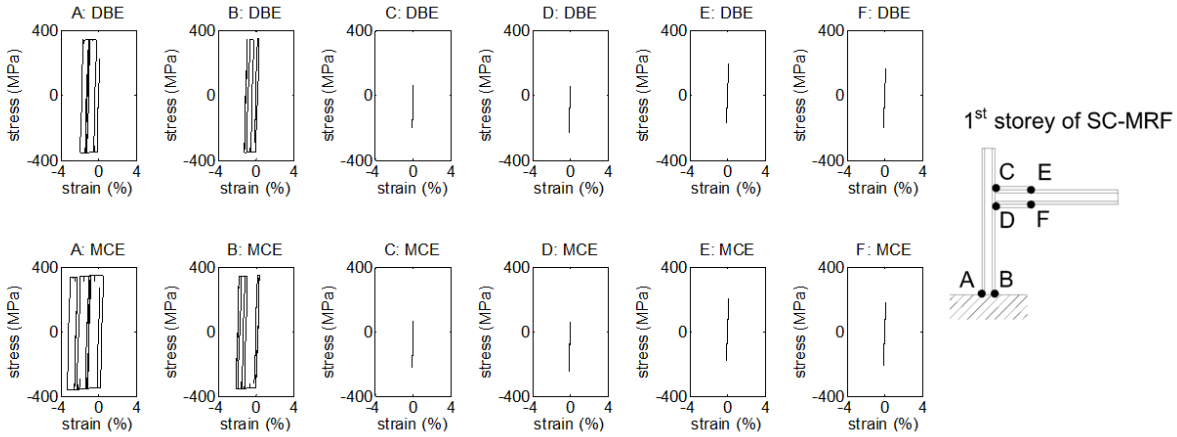

Figure 15: Stress-strain hysteresis at points A, B, C, D, E and F of the SC- MRF under the 5083-235 ground motion scaled at the DBE and MCE

Fig. 16 shows μ, μ + σ and median $\theta_{s\text{-}max}$ values under the earthquake ground motions of Table 2 scaled to the FOE, DBE and MCE. The μ, μ + σ and median height-wise $\theta_{s\text{-}max}$ distributions show identical shapes. The MRF has the largest $\theta_{s\text{-}max}$ in the fourth storey with μ values equal to 0.75% under the FOE, 1.65% under the DBE and 2.2% under the MCE, i.e., close to the design values of 0.64% under the FOE and 1.6% under the DBE, and, smaller than the design value of 2.4% under the MCE. The SC-MRF has the largest $\theta_{s\text{-}max}$ in the fourth storey with mean values equal to 0.75% under the FOE, 1.8% under the DBE and 2.5% under the MCE, i.e., slightly larger than the DBE and MCE design ones. Fig. 17 shows μ, μ + σ and median values of the residual storey drifts, $\theta_{s\text{-}res}$. $\theta_{s\text{-}res}$ show a uniform height-wise distribution for the conventional MRF and large dispersion compared to that of $\theta_{s\text{-}max}$. The largest $\theta_{s\text{-}res}$ of the conventional MRF occurs in the first storey with mean values equal to 0.1% under the DBE and 0.3% under the MCE. The associated μ + σ $\theta_{s\text{-}res}$ values are equal to 0.25% under the DBE and 0.6% under the MCE. The latter $\theta_{s\text{-}res}$ values indicate that repair of damage in the conventional MRF would be costly and disruptive after the DBE and not financially viable after the MCE (Mc Cormick et al. 2008). These results highlight the need for Eurocode 8 to include residual deformations as an additional seismic performance parameter. The SC-MRF practically eliminates residual storey drifts apart from the first storey that has μ and μ + σ $\theta_{s\text{-}res}$ values equal to 0.1% and 0.15% under both the DBE and MCE. The latter $\theta_{s\text{-}res}$ values are lower than the global sway imperfections defined in [8] and so it can be assumed that there will be no need for these residual drifts to be straightened out. Fig. 17 shows small μ + σ $\theta_{s\text{-}res}$ values in the third storey of the SC-MRF due to modest yielding in the beam ends.

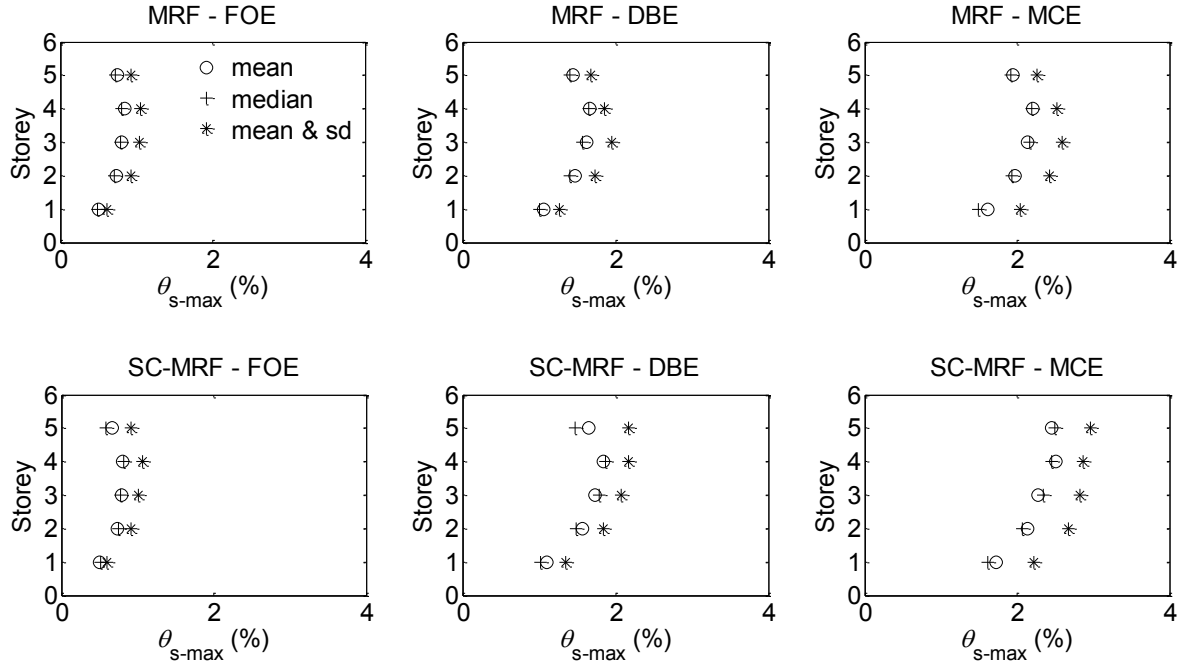

Figure 16: Statistics of peak storey drifts of the conventional MRF and the SC-MRF under 20 earthquake ground motions scaled to the FOE, DBE and MCE

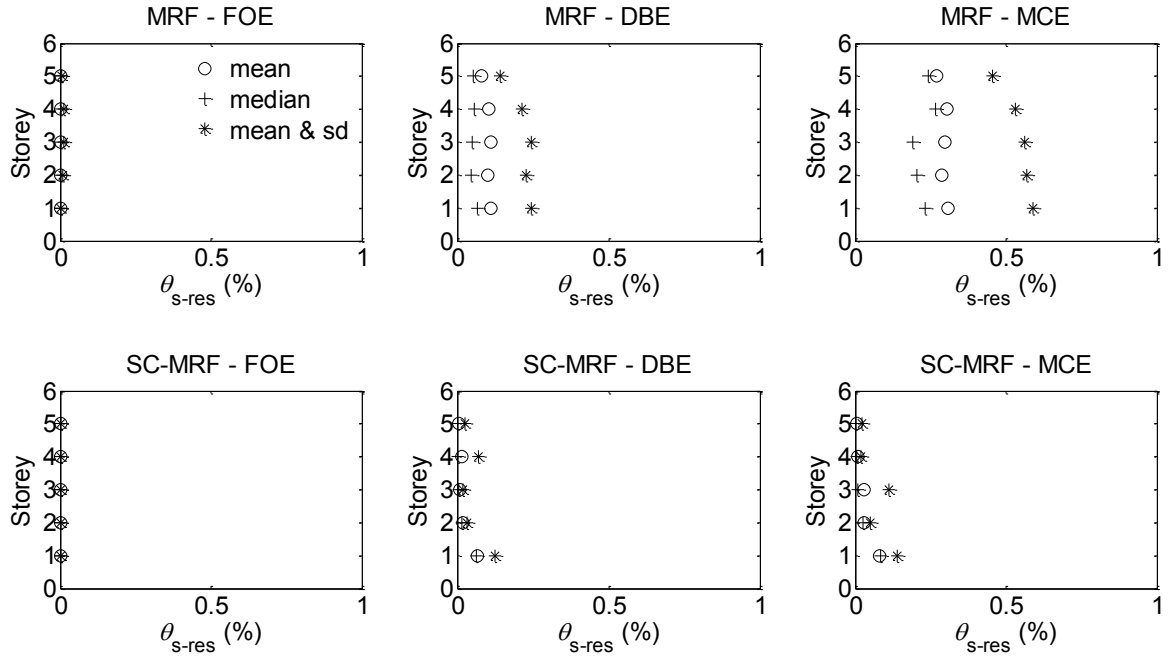

Figure 17: Statistics of residual storey drifts of the conventional MRF and the SC-MRF under 20 earthquake ground motions scaled to the FOE, DBE and MCE

9 SUMMARY AND CONCLUSIONS

This paper presented research on design, modelling and assessment of self-centering steel moment-resisting frames (SC-MRFs) using a recently developed post-tensioned (PT) connection with web hourglass shape steel pins (WHPs). The connection isolates inelastic deformations in WHPs, avoids damage in other connection parts as well as in beams and columns, and eliminates residual drifts. WHPs do not interfere with the composite slab and can be easily repaired without bolting or welding. A simplified nonlinear model has been developed for the PT connection with WHPs and the associated beams and columns. The model consists of nonlinear beam-column elements, and hysteretic and contact zero-length spring elements appropriately placed in the beam-column interface. A prototype building was designed as a conventional steel MRF according to Eurocode 8 or as a steel SC-MRF using PT connections with WHPs. Nonlinear models were developed in OpenSees for the two frames and used to conduct static monotonic (pushover), static cyclic (push-pull) and dynamic (seismic) analyses. Seismic analyses were conducted under a set of ground motions scaled to the frequently occurred, design basis and maximum considered earthquake intensities (FOE, DBE and MCE). Based on the results presented in this paper, the following conclusions are drawn:

- The proposed model for the PT connection with WHPs and the associated beams and columns has been calibrated against experimental results and found to accurately simulate the hysteretic behaviour of the PT connection. Papers should be written following the format of the Latex or Word macros for submission that can be found at the conference website.
- The design process for the prototype building resulted in the same beam and column cross sections for the conventional MRF and the SC-MRF. In addition, the WHPs and the required beam flange reinforcing plates of the SC-MRF have practical sizes. Deadline for the submission of papers posted in the website must be respected.
- Nonlinear static monotonic (pushover) analysis shows that the conventional MRF and the SC-MRF have comparable base shear strength and initial stiffness. The conventional

MRF experiences significant damage in beams at the DBE drift. On the other hand, the SC-MRF has damage-free beams for drifts even higher than the MCE drift.

- Nonlinear static cyclic (push-pull) analysis shows that the SC-MRF has full re-centering capability and adequate energy dissipation capacity under the DBE.
- Seismic analyses show that the conventional MRF and the SC-MRF have comparable peak storey drifts. In particular, the conventional MRF has slightly lower peak storey drifts than the SC-MRF. For both frames though the mean peak storey drifts are close to the design values.
- Seismic analyses show that the SC-MRF practically eliminates residual storey drifts apart from the first storey which sustains small residual drifts due to plastic deformations at the column bases. The mean plus one standard deviation value of the first storey residual drift of the SC-MRF is equal to 0.15% under both the DBE and MCE which is considered small and does not need to be straightened out.
- Seismic analyses show that the mean plus one standard deviation value of the maximum residual storey drift of the conventional MRF is 0.25% under the DBE and 0.6% under the MCE. These values indicate that repair of damage in the conventional MRF would be costly and disruptive after the DBE and not financially viable after the MCE.
- Seismic analyses show that the beams of the SC-MRF do not exhibit any yielding even under the MCE, while significant inelastic deformations are developed in the beams of the MRF under both the DBE and MCE. On the other hand, the column bases of the SC-MRF experience larger inelastic deformations than those of the conventional MRF.

REFERENCES

[1] AISC, Seismic provisions for structural steel buildings, Chicago, Illinois, 2005.

[2] F.A. Charney, W.M. Downs, Connections in steel structures, *V. ESSC/AISC Workshop*, Amsterdam, June 3-4, 2004.

[3] C.C Chou, J.H Chen, Y.C Chen and K.C Tsai, Evaluating performance of post-tensioned steel connections with strands and reduced flange plates, *Earthquake Engineering and Structural Dynamics* **35(9):** 1167-1185, 2006.

[4] C.C. Chou, Y.J. Lai, Post-tensioned self-centering moment connections with beam bottomflange energy dissipators, *Journal of Constructional Steel Research* **65**(10-11): 1931-1941, 2009.

[5] C.C Chou, K.C. Tsai, W.C Yang, Self-centering steel connections with steel bars and a discontinuous composite slab, *Earthquake Engineering and Structural Dynamics* **38**:403-422, 2009.

[6] C. Christopoulos, A. Filiatrault, C.M. Uang, B. Folz, Posttensioned energy dissipating connections for moment-resisting steel frames, *Journal of Structural Engineering* **128(9)**: 1111-1120, 2002b

[7] Eurocode 8, Design of structures for earthquake resistance - part1: General rules, seismic actions and rules for buildings, 2009

[8] Eurocode 3: Design of steel structures - part 1-1: General rules and rules for buildings, 2010

[9] Eurocode 1: Actions on structures - part 1-1: General actions densities, self weight and imposed loads, 2009

[10] M. Garlock, J.M. Ricles, R. Sause R, Experimental studies of full-scale posttensioned steel connections, *Journal of Structural Engineering* **131(3)**: 438-448, 2005

[11] M. Garlock, R. Sause, J.M. Ricles, Behavior and design of posttensioned steel frame systems, *Journal of Structural Engineering* **133(3)**: 389-399, 2009.

[12] T.L. Karavasilis, C.Y. Seo, Seismic structural and non-structural performance evaluation of highly-damped self-centering and conventional systems, *Engineering Structures* **33(8)**: 2248-2258, 2011.

[13] T.L. Karavasilis, J.M. Ricles, R. Sause, C. Chen, Experimental evaluation of the seismic performance of steel MRFs with compressed elastomer dampers using large-scale real-time hybrid simulation, *Engineering Structures* **33(6)**:1859-1869, 2011

[14] T.L. Karavasilis, S. Kerawala, E. Hale, Model for hysteretic behaviour of steel energy dissipation devices and evaluation of a minimal-damage seismic design approach for steel frames, *Journal of Constructional Steel Research* **70**:358-367, 2012.

[15] H.J. Kim, C. Christopoulos, Friction damped posttensioned self-centering steel moment-resisting frames, *Journal of Structural Engineering* **134(11)**: 1768-1779, 2008a.

[16] H.J. Kim, C. Christopoulos, Seismic design procedure and seismic response of post-tensioned self-centering steel frames, *Earthquake Engineering and Structural Dynamics* **38(3)**: 355-376, 2008b

[17] T. Kobori, Y. Miura, E. Fukuzawa, T. Yamada, T. Arita, Y. Takenaka, N. Miyagawa, N. Tanaka N, T. Fukumoto, Development and application of hysteresis steel dampers, *Earthquake Engineering, Tenth World Conference*, Rotterdam: Balkema, 1992.

[18] S. Mazzoni, F. McKenna, M. Scott, G. Fenves, Open system for earthquake engineering simulation (OpenSees). User Command Language Manual, Pacific Earthquake Engineering Research Center, University of California, Berkeley, 2006.

[19] J. Mc Cormick, H. Aburano, M. Ikenaga, M. Nakashima, Permissible residual deformation levels for building structures considering both safety and human elements, *14th WCEE, Beijing, China*, 2008.

[20] J. Ricles, R. Sause, M. Garlock, C. Zhao, Posttensioned seismic-resistant connections for steel frames, *Journal of Structural Engineering* **127(2)**: 113-121, 2001

[21] J. Ricles, R. Sause, S.W. Peng, L.W. Lu, Experimental evaluation of earthquake resistant posttensioned steel connections, *Journal of Structural Engineering* **128(7)**: 850-859, 2002.

[22] P. Rojas, J.M. Ricles, R. Sause R, Seismic performance of post-tensioned steel moment resisting frames with friction devices, *Journal of Structural Engineering* **131(4)**: 529-540, 2004.

[23] P. Somerville, Development of ground motion time histories for phase 2 of the FEMA/SAC steel project, Report No. SAC/DB-97/04, Sacramento, CA, 1997.

[24] K.C. Tsai, C.C. Chou, C.L. Lin, P.C. Chen, S.J. Jhang SJ, Seismic self-centering steel beam-to-column moment connections using bolted friction devices, *Earthquake Engineering and Structural Dynamics* **37**: 627-645, 2008.

[25] G. Vasdravellis, T.L Karavasilis, B. Uy, Large-scale experimental validation of steel post-tensioned connections with web hourglass pins, *Journal of Structural Engineering*, in press, 2012.

[26] G. Vasdravellis, T.L. Karavasilis, B. Uy, Finite element models and cyclic behaviour of self-centering steel post-tensioned connections with web hourglass pins, *Engineering Structures*, in press, 2013.

[27] J. Whittle, M.S. Williams, T.L. Karavasilis, T. Blakeborough, A comparison of viscous damper placement methods for improving seismic building design, *Journal of Earthquake Engineering* **16**:540-560, 2012.

[28] M. Wolski, J.M. Ricles, R. Sause, Experimental study of a self-centering beam-column connection with bottom flange friction device, *Journal of Structural Engineering* **135(5)**: 479-488, 2009.